

# Extrinsic Limitations of Stealthy Hyperuniform Optical Metasurfaces

Y. Xu<sup>1</sup>, M. Chen<sup>1</sup>, L. Forestier<sup>1</sup>, F. Carcenac<sup>2</sup>, L. Mazenq<sup>2</sup>, and P. Lalanne<sup>1\*</sup>

<sup>1</sup>Laboratoire Photonique Numérique et Nanosciences (LP2N), Université de Bordeaux, Institut d'Optique Graduate School, CNRS, Talence, France

<sup>2</sup>LAAS-CNRS, Université de Toulouse, CNRS, Toulouse, France

\*Corresponding author: [Philippe.Lalanne@institutoptique.fr](mailto:Philippe.Lalanne@institutoptique.fr)

**Abstract:** Hyperuniform metasurfaces promise an unusual form of wave control: the suppression of elastic scattering over extended angular ranges without periodic order. Here, we present a comprehensive experimental and theoretical study of 2D stealthy hyperuniform metasurfaces operating at optical frequencies. In agreement with theoretical expectations, we observe a pronounced reduction of elastic scattering around the specular direction in metasurfaces fabricated by electron-beam lithography. However, the measured suppression is substantially weaker than that predicted by structure-factor calculations based on ideal stealthy hyperuniform point-pattern generators. We identify and quantitatively analyze the physical origins of this discrepancy, and establish realistic performance bounds. By isolating the dominant limiting mechanisms, our results provide practical design guidelines for the implementation of stealthy hyperuniform metasurfaces in functional photonic devices.

## 1. Introduction

The study of light propagation in complex media has been an active field for several decades, stimulating fundamental questions in mesoscopic physics [1] and enabling a wide range of photonic applications [2]. More recently, the ability to engineer disorder through controlled structural correlations has opened new avenues for designing materials with tailored optical responses [3-9].

Hyperuniformity [10,11] is a general concept introduced to characterize a class of correlated disordered systems that exhibit a pronounced suppression of density fluctuations at large length scales, while remaining disordered at short scales. This concept has found applications across diverse fields, ranging from photonic materials [12,13], as considered here, to biological systems [14] and cosmology [15]. Formally, hyperuniform point patterns are characterized by structure factors  $S_r$  that vanish as the wavelength tends to infinity,  $S_r(\mathbf{q}) \rightarrow 0$  as the reciprocal wavevector  $\mathbf{q}$  tends towards zero.

In this work, we investigate *stealthy hyperuniform* structures (SHU), a special subclass of hyperuniform systems in which density fluctuations are completely suppressed over a finite domain of reciprocal space, i.e.  $S_r(\mathbf{q}) = 0$  for all  $|\mathbf{q}|$  smaller than a prescribed cutoff  $q_{\max}$ .

We focus on two-dimensional (2D) hyperuniform metasurfaces rather than three-dimensional metamaterials, since planar geometries are naturally compatible with standard nanofabrication techniques and allow accurate control of metaatom positions. Accordingly, we consider diffraction by metasurfaces rather than transport in bulk media[16-19], a regime that has received comparatively little experimental attention [20,21]. In this geometry,  $\mathbf{q}$  denotes the in-plane wavevector component  $\mathbf{q}_{\parallel} = [q_x, q_y]$  parallel to the surface.

Within scattering theory,  $\mathbf{q}_{\parallel}$  corresponds to the in-plane momentum transfer between the scattered and incident plane waves and stealthy hyperuniformity is expected to strongly inhibit

elastic scattering over a well-defined angular range around the specular light direction  $\mathbf{q}_{\parallel} = \mathbf{0}$  (Figure 1). We define the quenching zone as the finite region of momentum space over which this inhibition occurs, and the quenching efficiency as the reduction in scattered intensity per solid angle inside the quenching zone relative to outside it. These quantities provide a direct figure of merit for applications requiring controlled angular response.

Several algorithms [16,22-24] have been developed to generate hyperuniform point patterns that exhibit extremely large theoretical quenching efficiencies, typically exceeding  $10^5$ . These algorithms are both effective and highly flexible, as they can be extended to anisotropic configurations exhibiting distinct responses along the  $q_x$  and  $q_y$  directions [25]. The spatial extent of the quenching region is predicted to depend on parameters such as the wavelength and metaatom density, through a relation referred to as the quenching equation hereafter by analogy with the grating equation for periodic surfaces.

Using metasurfaces fabricated by electron-beam lithography, we provide an experimental and quantitative validation of this quenching equation and assess the attainable quenching efficiencies under realistic conditions. We show that theoretical efficiencies substantially overestimate the values achievable in experiments.

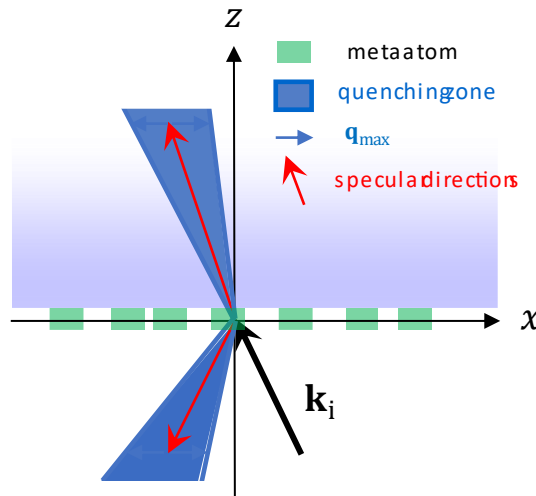


**Figure 1.** Quenching zone of stealthy hyperuniform metasurfaces illuminated by an incident oblique planewave with a wavevector  $\mathbf{k}_i = [\mathbf{k}_{i,\parallel}, k_{i,z}]$ . Around the specular directions (red arrows) defined by  $\mathbf{k}_{s,\parallel} = \mathbf{k}_{i,\parallel}$ , no light is scattered in a cone defined by in-plane wavevectors  $\mathbf{k}_{i,\parallel} + \mathbf{q}_{\parallel}$ , such as  $|\mathbf{q}_{\parallel}| < q_{\max}$ .

There are several reasons why the strong quenching predicted theoretically by the structure factor may not be observed experimentally. To identify them, let us consider a metasurface composed of a collection of  $N$  metaatoms, located in the plane  $z = 0$  at positions  $\mathbf{r}_p = [\mathbf{r}_{p,\parallel}, z_p = 0]$ , with  $p = 1 \dots N$ . The metasurface is illuminated by a planewave with a wavevector  $\mathbf{k}_i = [\mathbf{k}_{i,\parallel}, k_{i,z}]$ .

We consider the field scattered into a plane wave with wavevector  $\mathbf{k}_s = [\mathbf{k}_{s,\parallel}, k_{s,z}]$  and define the in-plane momentum transfer  $\mathbf{q}_{\parallel} = \mathbf{k}_{s,\parallel} - \mathbf{k}_{i,\parallel}$ . The total scattered electric field can be written as a superposition of the fields,  $\mathbf{E}_s^{(p)}(\mathbf{r})$ , scattered by the individual metaatoms,

$$\mathbf{E}_s(\mathbf{r}) = \sum_{p=1}^N \mathbf{E}_s^{(p)}(\mathbf{r}) \exp[-i\mathbf{q}_{\parallel} \cdot \mathbf{r}_{p,\parallel}], \quad (1)$$

where the exponential factor  $\exp[-i\mathbf{q}_{\parallel} \cdot \mathbf{r}_{p,\parallel}]$  is a dephasing term between the incident and scattered planewaves and is introduced for convenience. A common simplifying assumption is

that all metaatoms scatter identically, such that  $\mathbf{E}_s^{(p)} = \mathbf{E}_s^{(0)}(\mathbf{r})$  for all  $p$ . Under this assumption, the scattered field factorizes as  $\mathbf{E}_s(\mathbf{r}) = \mathbf{E}_s^{(0)}(\mathbf{r}) \sum_{p=1}^N \exp[-i\mathbf{q}_{\parallel} \cdot \mathbf{r}_{p,\parallel}]$ , and the interference sum,  $\sum_{p=1}^N \exp[-i\mathbf{q}_{\parallel} \cdot \mathbf{r}_{p,\parallel}]$ , then plays a central role. Upon taking the modulus squared to obtain the scattered intensity, this term gives rise to the structure factor [20],

$$S_r(\mathbf{q}_{\parallel}) = \frac{1}{N} \left| \sum_{p=1}^N \exp[-i\mathbf{q}_{\parallel} \cdot \mathbf{r}_{p,\parallel}] \right|^2. \quad (2)$$

Any deviation from the condition,  $\mathbf{E}_s^{(p)}(\mathbf{r}) = \mathbf{E}_s^{(0)}(\mathbf{r})$  for all  $p$ , prevents the structure factor to accurately imprint its signature on the actual properties of the diffuse light. Two primary mechanisms can lead to such deviations:

- Polydispersity. When the metaatoms are not strictly identical, there is no reason to expect them to scatter light in the same manner, resulting in a breakdown of the factorization assumption.
- Multiple scattering. Even for perfectly identical metaatoms, the local excitation field differs from site to site because it includes contributions from waves scattered by all other metaatoms. Multiple scattering effects can therefore be neglected only in sufficiently dilute metasurfaces.

An additional limitation arises from finite-size effects imposed by experimental constraints, such as the finite spatial coherence of the incident beam or the finite lateral extent of the metasurface.

By systematically identifying and quantifying the dominant limiting mechanisms, we establish realistic performance bounds for stealthy hyperuniform metasurfaces and clarify their potential for practical photonic applications.

## 2. Experimental results

**SHU pattern generation.** We have adapted the algorithms introduced in [16,26], which is based on minimizing an interaction potential, to generate two-dimensional SHU point patterns under periodic boundary conditions (Figure 2(a)). The key quantities and definitions used by the SHU point-pattern generators are briefly recalled below.

We consider a 2D lattice of  $N$  points located within a square domain of side length  $L$  and impose periodic boundary conditions. Due to periodicity, the allowed wavevectors form a square lattice with spacing  $\Delta q_x = \Delta q_y = 2\pi/L$  and the structure factor is nonnull only at this discrete momentum values. The SHU point-pattern generator optimizes the position of the  $N$  points under the constrain that the structure factor is almost null for a finite number of reciprocal lattice vectors inside a disc of radius  $q_{\max}$  in the reciprocal space. The number of constrained wave vectors,  $M(q_{\max})$ , depends on the radius  $q_{\max}$  and is given by  $2M(q_{\max}) + 1 = \pi(q_{\max}/2\Delta k)^2$  [26,27].

The degree of order in the pattern is quantified by the parameter  $\chi = M(q_{\max})/2N$ , commonly referred to as the degree of stealthiness. When  $\chi = 0$ , the arrangement is completely random and unconstrained. For  $\chi > 0.5$ , the pattern increasingly approaches a highly ordered polycrystalline structure (see Figure 2(a)). When  $\chi = 1$ , all points are fully constrained, corresponding to a perfect lattice. Using the definition of  $\chi$ , one can relate the threshold wavenumber  $q_{\max}$  to the degree of stealthiness, leading to the quenching equation [11]

$$q_{\max} = \sqrt{(4N\chi + 1)/\pi} \Delta k \approx 4\sqrt{\pi\rho\chi}. \quad (3)$$

where  $\rho = N/L^2$  is the point density.

Figure 2(b) displays an example of structure factor computed for a periodic SHU pattern for  $\chi = 0.35$ . Inside the disc defined by  $|\mathbf{q}| < q_{\max}$ , the structure factor is  $\approx 10^5$  times smaller than outside.

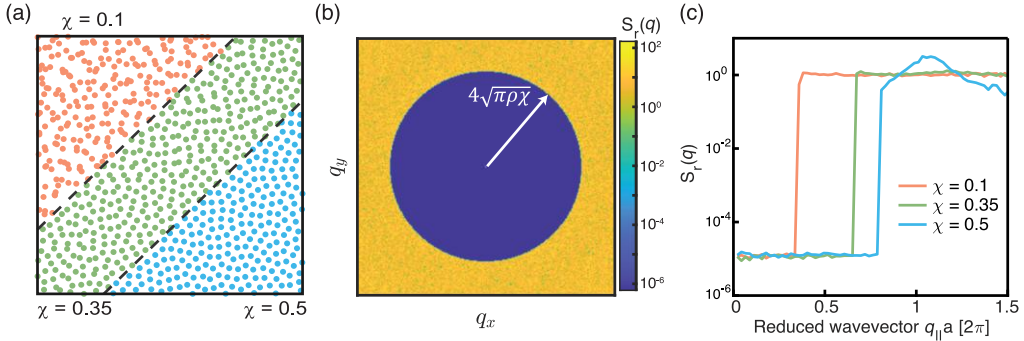


**Figure 2.** Generation of SHU patterns. (a) Examples of spatial point patterns with three different degrees of stealthiness,  $\chi = 0.1$ ,  $\chi = 0.35$  and  $\chi = 0.5$ , at fixed particle density. (b) Structure factor of a SHU periodic pattern with  $N = 20,000$  points containing  $\chi = 0.35$ . (c) Radially averaged structure factors for a SHU periodic pattern with  $N = 20,000$  points for different  $\chi$  values. The horizontal axis represents the reduced in-plane wavevector modulus,  $q_{\parallel}a$ , where  $a = 1/\sqrt{\rho}$  is the characteristic length scale.

Three subsets of three generated SHU patterns for  $\chi = 0.1$ ,  $0.35$  and  $0.5$  with 20,000 points are presented in Figure 2(a). Although the optimization algorithm operates in Fourier space to adjust the point positions—thereby imposing long-range correlations—increasing  $\chi$  leads to point arrangements that exhibit short-range correlations. The corresponding radially averaged structure factors are shown in Figure 2(c). Within the quenching zone, the structure factor reaches minimum values on the order of  $10^{-5}$ .

**Metasurfaces fabrication.** The hyperuniform metasurfaces are fabricated using electron-beam lithography in a negative-tone resist, followed by pattern transfer into a 145-nm-thick silicon layer deposited on a glass substrate. More details can be found in [28].

SHU point patterns were generated for degrees of stealthiness  $\chi$  ranging from 0.1 to 0.6 and number densities  $\rho$  ranging from  $2 \mu\text{m}^{-2}$  to  $4 \mu\text{m}^{-2}$ . The area of each generated pattern was fixed at  $100 \times 100 \mu\text{m}^2$ . To achieve the target density, the total number of points  $N$  was adjusted accordingly. Each pattern was used as a unit cell and tiled into a  $3 \times 3$  array, resulting in nine replicated copies. The point coordinates were exported in Graphic Data System (GDS) format for lithographic fabrication. Consequently, all fabricated metasurfaces are square, with lateral dimensions of 300  $\mu\text{m}$ .

This fabrication yields a comprehensive library of SHU metasurfaces with systematically varied metaatom lateral size  $l$ , density  $\rho$ , and degree of stealthiness  $\chi$ . Figure 3(a) presents scanning electron microscope (SEM) images of two representative samples with  $\chi = 0.1$  and  $\chi = 0.5$ , both at a density of  $\rho = 2 \mu\text{m}^{-2}$  for  $l = 100 \text{ nm}$ . Insets in the bottom-left corner show the corresponding microscopic bright-field images. SEM images of the full set of fabricated metasurfaces are provided in Figure S5.

**Experimental verification of the quenching equation.** Under the independent scattering approximation, the scattered intensity from a metasurface is proportional to the product of the structure factor and the form factor of the metaatoms [20]. The form factor corresponds to the differential scattering cross section of an individual metaatom. This description is directly analogous to X-ray and neutron scattering experiments, in which the scattering patterns of solids are determined by the interplay between structure and form factors.

The spectrally and angularly resolved scattered light from the metasurfaces is measured using a gonio-spectrometer setup (Figure S1) combined with a slightly focused supercontinuum laser,

which ensures almost uniform illumination across the metasurface area. Owing to the isotropic nature of the metasurfaces, scattering is collected as a function of the polar detection angle. After normalization to the diffuse response of a reference diffuser with Lambertian reflectance, the measurements yield the bidirectional reflectance distribution function (BRDF) [29].

Figure 3(b) shows the BRDF as a function of detection (polar) angle for three SHU metasurfaces of different densities and degrees of stealthiness under normal incidence at a wavelength of 480 nm. Within the angular range from  $0^\circ$  to  $\theta_{\max}$ , diffuse scattering is strongly suppressed. The width of the quenching scattering zone depends on either the density or the degree of stealthiness and is governed by the quenching equation [Equation (3)], which can be rewritten under normal incidence at wavelength  $\lambda$  as

$$\sin(\theta_{\max}) = 2\sqrt{\rho\chi/\pi}\lambda, \quad (4)$$

showing that  $\sin(\theta_{\max})$  depends linearly on the incident wavelength, with a slope determined by  $\sqrt{\rho\chi}$ .

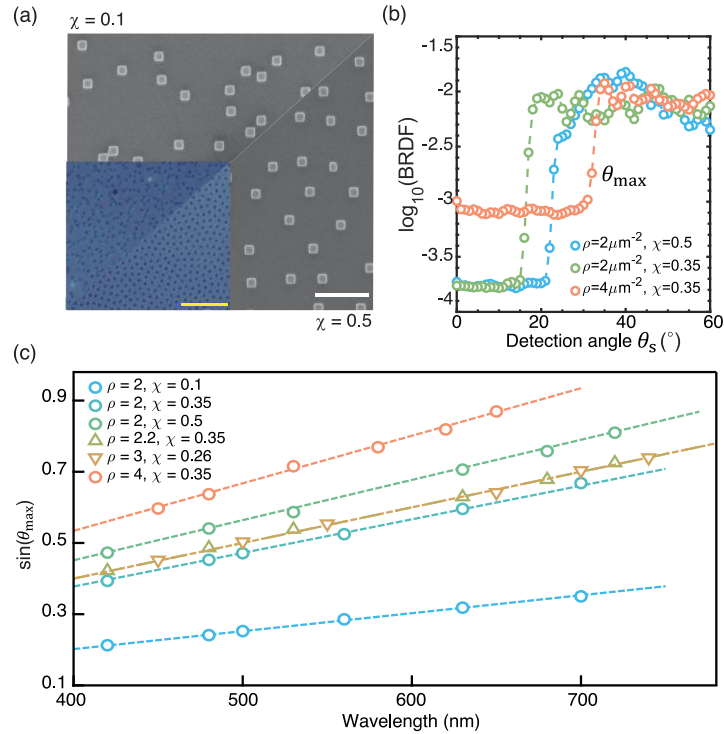


**Figure 3.** Verification of the quenching equation. (a) SEM images and corresponding optical microscope images of two samples with  $\chi = 0.1$  and  $\chi = 0.5$  for the same particle density  $\rho = 2 \mu\text{m}^{-2}$ . Scale bar for SEM:  $1\mu\text{m}$ , scale bar for microscope images:  $5\mu\text{m}$ . (b) Examples of measured BRDFs as a function of scattering angle  $\theta_s$  at a wavelength of  $\lambda = 480 \text{ nm}$ . (c) Verification of the quenching equation for different metasurfaces. Dashed curves denote the theoretical predictions of Equation (4), while scatter points indicate the threshold values extracted from the BRDF measurements.

To validate Equation (4), the transitioning angle  $\theta_{\max}$  extracted from measurements performed at various wavelengths for various SHU metasurfaces are shown in Figure 3(c). The experimentally extracted values are indicated by circles and triangles, while the dashed curves correspond to Equation (4) using the respective values of  $\rho$  and  $\chi$ . Excellent agreement is observed for all metasurfaces. Notably, for the two metasurfaces indicated by triangles, the products  $\rho\chi$  are identical  $\rho\chi = \pi/4 [\mu\text{m}^{-2}]$ , resulting in the same slope, and, consequently, overlapping curves. This demonstrates that the quenching zone can be controlled using two independent parameters,  $\rho$  and  $\chi$ , provided their product remains constant.

Together, Equation (3) or Equation (4) provide a practical and intuitive framework for engineering the angular distribution of diffuse scattering, which is of central importance for a wide range of photonic applications, including solar cells [30], solid-state lighting devices [7] and colored surfaces in architecture and design [28].

**Quenching efficiency.** Despite the good agreement in the angular position of the quenching transition, Figure 3(b) reveals pronounced differences in quenching efficiency among the investigated samples. In particular, the experimentally observed quenching efficiencies, typically ranging from 10 to 100, are orders of magnitude weaker than those theoretically predicted with the structure factor. Other BRDF measurements with other metasurfaces with different metaatom lateral dimensions (see Figure S3) further confirm that the theoretical quenching efficiencies are experimentally unattainable.

### 3. Finite size effect

Although the SHU patterns are generated under periodic boundary conditions, fabrication and measurement constraints inevitably introduce finite-size effects. Finite size may arise, for example, from the finite aperture of the metasurface. Moreover, even in spatially extended systems, the constructive and destructive interference underlying the structure factor is fundamentally limited by the spatial coherence of the illumination. This limitation is particularly relevant for applications such as solar cells [30], where the spatial coherence length of sunlight is finite and typically on the order of tens of micrometers[31].

In finite-size systems, a continuum of wavevectors lying between the quantized, reciprocal-space constrained wavevectors,  $\mathbf{q} = [n_x(2\pi/L), n_y(2\pi/L)]$  with  $n_x$  and  $n_y$  being relative integers, become accessible. These intermediate wavevectors are not explicitly constrained by the hyperuniform pattern-generation algorithm, and their associated structure factors can therefore exceed the target optimized values.

Our objective is to quantify the impact of this unconstrained continuum of wavevectors on the quenching efficiency. We begin with a step-by-step analysis of SHU patterns containing a small number  $N$  of points (Figure 4(a)–(c)) and subsequently summarize the behavior for large  $N$  in Figure 4(d).

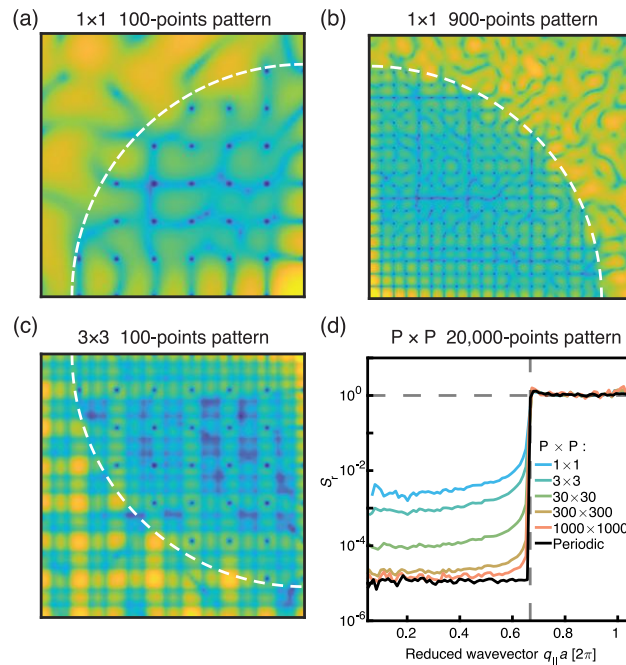


**Figure 4.** Effect of finite size on the structure factor  $S_r$ . (a)  $S_r$  of a single unit cell containing  $N = 100$  points. Small values of  $S_r$  occur only at quantized wavevectors,  $\mathbf{q} = n_x(2\pi/L)\hat{x} +$

$n_y(2\pi/L)\hat{\mathbf{y}}$ . (b)  $S_r$  of a single unit cell containing  $N = 900$  points;  $S_r$  still has large values between the quantized wavevectors. (c)  $S_r$  of a  $3 \times 3$  replication of the unit cell shown in (a). (d) Structure factors obtained for  $P \times P$  replications of an initial unit cell with  $N = 20,000$  points, for  $P = 1, 3, 30, 300, 1000$  and  $\infty$  (periodic limit). Very large quenching efficiencies close to the periodic case are obtained significant  $P$  values, typically  $P > 300$ . All computations are performed for stealthy hyperuniform patterns corresponding to  $\chi = 0.35$ .

Figure 4(a) shows the computed structure factor of a single SHU unit cell containing  $N = 100$  points. Even within the quenching zone indicated by the white dashed arc, small values of  $S_r$  occur only at the quantized wavevectors imposed by periodic boundary conditions. The unconstrained continuum of wavevectors exhibits significantly larger values—at least four orders of magnitude higher—which dominate upon momentum-space averaging and therefore drastically reduce the quenching efficiency.

Figure 4(b) corresponds to a larger number of points,  $N = 900$ . In this case, the constrained wavevectors are more densely distributed within the quenching zone. As a result, the structure factor takes smaller values throughout the unconstrained continuum, leading to an increase in the averaged quenching efficiency with increasing  $N$ .

In practice, however, algorithmic limitations make it difficult to indefinitely increase the number of points  $N$  in a single SHU unit cell to further suppress the contribution of the unconstrained continuum of wavevectors. A commonly adopted alternative is therefore to replicate a smaller SHU unit cell.

Consider a finite-size pattern formed by tiling  $P_x \times P_y$  identical replications of a unit cell of size  $L \times L$ . Denoting by  $S_{1 \times 1}$  the structure factor of a single unit cell, the structure factor of the tiled pattern,  $S_{P_x \times P_y}(\mathbf{q})$ , is given by [32,26]

$$S_{P_x \times P_y}(\mathbf{q}) = S_{1 \times 1}(\mathbf{q}) \times \frac{1}{P_x P_y} \left| \frac{\sin(P_x L \mathbf{q} \cdot \hat{\mathbf{x}}/2)}{\sin(L \mathbf{q} \cdot \hat{\mathbf{x}}/2)} \frac{\sin(P_y L \mathbf{q} \cdot \hat{\mathbf{y}}/2)}{\sin(L \mathbf{q} \cdot \hat{\mathbf{y}}/2)} \right|^2. \quad (5)$$

The sinc-like term represents the familiar interference factor arising from the Cartesian tiling of multiple unit cells. Equation (5) shows that, in the limit  $P_x, P_y \rightarrow \infty$ , the structure factor becomes nonzero only at the discrete wavevectors  $\mathbf{q} = \left(\frac{2\pi n_x}{L}, \frac{2\pi n_y}{L}\right)$ ,  $n_x, n_y \in \mathbb{Z}$ , which coincide with those constrained by the pattern-generation algorithm through periodic boundary conditions (see Figure S4).

Figure 4(c) shows the structure factor obtained from a  $3 \times 3$  replication of the SHU unit cell shown in Figure 4(a). Compared to Figure 4(a), the structure factor at unconstrained wavevectors is substantially larger. As the number of replications increases toward infinity, the sinc-like term converges to a Dirac comb [32], such that only discrete wavevectors contribute to the structure factor, as illustrated in Figure 1(b).

The structures factors in Figure 4(b) and 4(c) correspond to the same total number of points. A direct comparison reveals that the tiled pattern exhibits a more contrasted structure factor with pronounced anisotropy. Therefore, for a fixed patterned area, generating a single unit cell containing a large number of points is preferable to tiling smaller unit cells, in order to achieve improved isotropy and smoother angular response.

Figure 4(d) summarizes these observations for unit cells containing  $N = 20,000$  points, corresponding to the patterns used in the experiment. It displays the radially averaged structure factor for metasurfaces composed of  $P \times P$  replications, with  $P = 1, 3, 30, 300, 1000$  and in the periodic limit  $P \rightarrow \infty$  (black curve). As expected, the quenching efficiency increases monotonically with  $P$ . However, quenching efficiencies approaching the periodic limit are obtained only for very large values of  $P$ . For reference, a metasurface composed of

$1000 \times 1000$  unit cells with  $N = 20,000$  points for a density of  $2 \mu\text{m}^{-2}$  would occupy an area of  $100 \times 100 \text{ mm}^2$ .

Fabricating metasurfaces of such dimensions is inherently challenging and achieving illumination with uniform intensity and phase over such an extended area places stringent requirements on the light source. We therefore conclude that the quenching efficiency predicted for ideal periodic systems is not achievable in practice. Under our experimental conditions ( $N = 20,000$  and  $P = 3$ ), finite-size effects limit the quenching efficiency to approximately  $10^3$  (blue-green curve in Figure 4(d)).

Since this value remains significantly larger than the experimentally observed quenching efficiencies (with a maximum of  $\sim 70$ , see Figure S3), additional mechanisms must be considered to explain the remaining discrepancy.

#### 4. Polydispersity effect

Electron-beam lithography enables metaatoms to be positioned with high accuracy, typically at the nanometer scale. However, proximity effects and variations in the etching process can induce small but finite deviations in shape and size, leading to metaatom-to-metaatom variations in the scattered electromagnetic field. In the presence of such variations, Equation (2), which assumes that the scattered fields from different metaatoms are identical, is not valid. Instead, polydispersity must be considered based on Equation (1). Under the independent scattering approximation, interactions between metaatoms manifest through interference of their far-field scattering, and the effect of polydispersity could therefore be considered in the far field.

Consider a single Si nanobox with size  $l$  illuminated by an incident plane wave. With near-to-far-field transformations, we can compute the planewave expansion of the far field scattered in the direction  $\mathbf{k}_s$  with polarization  $\alpha$ . We denote by  $\alpha^{(l)}(\mathbf{k}_s, \mathbf{k}_i, \alpha)$  the complex amplitude of this expansion [33]. Similarly, we can compute a reference complex amplitude  $\alpha^{(0)}(\mathbf{k}_s, \mathbf{k}_i, \alpha)$  for a reference metaatom size  $l_0$ . We further introduce  $\delta^{(l)}(\mathbf{k}_s, \mathbf{k}_i, \alpha) = \alpha^{(l)}(\mathbf{k}_s, \mathbf{k}_i, \alpha)/\alpha^{(0)}(\mathbf{k}_s, \mathbf{k}_i, \alpha)$ , a complex number which highlights the fluctuations of the far-field planewave amplitude for an incident wavevector  $\mathbf{k}_i$ , a scattered wavevector  $\mathbf{k}_s$  and a polarization  $\alpha$  due to fluctuations in metaatom sizes. Indeed, as the size fluctuation vanishes,  $\delta^{(l)} \rightarrow 1$ .

Including these fluctuations, analogous to Equation (1), for a collection of  $N$  metaatoms with in-plane position distribution  $\mathbf{r}_{p,\parallel}$  and size distribution  $l^{(p)}$ , the complex amplitude  $\alpha_c$  in the  $\mathbf{k}_s$  direction with polarization  $\alpha$  is given by

$$\alpha_c(\mathbf{k}_s, \mathbf{k}_i, \alpha) = \alpha^{(0)}(\mathbf{k}_s, \alpha) \sum_{p=1}^N \delta^{l^{(p)}}(\mathbf{k}_s, \mathbf{k}_i, \alpha) \exp[-i\mathbf{q}_\parallel \cdot \mathbf{r}_{p,\parallel}]. \quad (6)$$

Thus, compared with the monodisperse case, polydispersity can be incorporated by assigning to each metaatom a complex weight  $\delta^{l^{(p)}}$ , which fluctuates around unity. Thus, we can define a modified structure factor  $S_{\text{poly}}$  [34,35]

$$S_{\text{poly}}(\mathbf{k}_s, \mathbf{k}_i, \alpha) = \frac{1}{N} \left| \sum_{p=1}^N \delta^{l^{(p)}}(\mathbf{k}_s, \mathbf{k}_i, \alpha) \exp[-i\mathbf{q}_\parallel \cdot \mathbf{r}_{p,\parallel}] \right|^2, \quad (7)$$

which accounts for polydispersity and can be statistically averaged for a fixed set of  $\mathbf{r}_{p,\parallel}$ . Indeed, this result holds under the independent scattering approximation.

To investigate the effect of polydispersity, the statistical distributions of the lateral sizes of the Si nanoboxes were extracted from SEM images. Statistical analysis of 40 nanoboxes yields an average lateral size of  $l = 111.7 \pm 1.8 \text{ nm}$  (Figure 5(a)). Based on this size distribution, the

near-field scattered under normal incidence at  $\lambda = 532$  nm is computed using the open-source freeware RETOP [33] for a collection of nanoboxes with lateral sizes varying with a 1 nm step. At this wavelength, the refractive index of silicon was taken from experimentally measured values  $n_{\text{Si}} = 4.3 + 0.16i$ . In all computations, the phase origin is consistently chosen at the substrate interface at the center of the bottom face of each nanobox.

Because we consider in-plane scattering directions only (the azimuthal angle is null) and a TE polarized incident plane wave, owing to symmetry, the scattered plane wave is also TE polarized for all scattering directions. Figure S6 shows the phase and modulus of  $\delta^l$  for each scattering direction, normalized for a reference size  $l_0 = 112$  nm. Since the range of size variations is small and the trends are essentially the same all different scattering directions (Figure S6), we only plot the data computed at a polar angle of  $30^\circ$  in Figure 5(b).

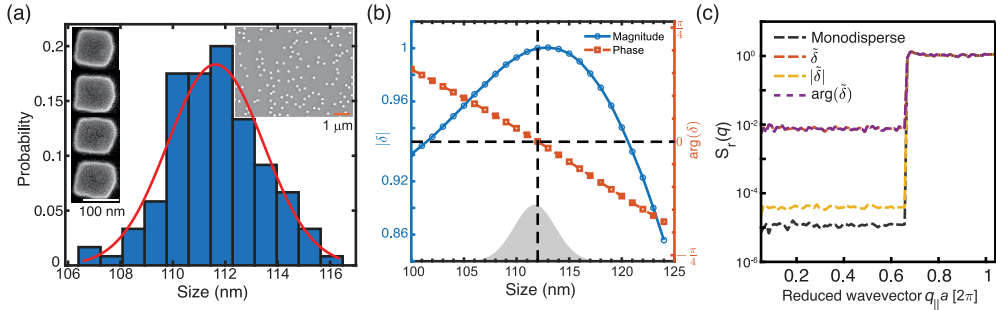


**Figure 5.** Effect of polydispersity on the structure factor. (a) Statistical distribution of nanobox sizes. Inset: SEM images; left scale bar: 100 nm, right scale bar: 1  $\mu\text{m}$ . (b) Simulated scattered-field fluctuations  $\delta^l$  for nanoboxes of different sizes, with amplitudes normalized to the complex amplitude of the average-size metaatom. Left: magnitude; Right: phase. (c) Polydisperse structure factor obtained by weighting with randomly distributed  $\delta^l$ .

Based on the experimentally extracted probability distribution, different sizes of Si nanoboxes are randomly assigned for the computation of the modified structure factor  $S_{\text{poly}}$  for  $N = 20,000$  points and  $\chi = 0.35$ . Figure 5(c) compares the structure factors for both monodisperse and polydisperse cases. Polydispersity reduces the quenching efficiency dramatically, from  $10^5$  to  $10^2$ .

To understand the origin of this large reduction, we computed the contributions of modulus and phase fluctuations to the structure factor separately. As shown in Figure 5(c), the phase fluctuations are primarily responsible for the observed change. Indeed, the phase varies rapidly around the reference size  $l_0$ . We attribute this rapid variation to a resonance of the metaatom, which is further supported by the observation in Figure 5(b) of the initial increase followed by a subsequent decrease in  $|\delta^l|$ .

We conclude that both finite-size effects and polydispersity lead to a substantial reduction in quenching efficiency, from  $10^5$  to  $10^2$ . However, these factors alone are insufficient to explain two key experimental observations. First, the measured quenching efficiency, typically slightly above  $10^1$ , remains far below the values predicted when accounting only for finite-size and polydispersity effects. Second, the experimentally observed quenching efficiency decreases with increasing metaatom density, even though a higher density corresponds to a larger number of points and would be expected to yield higher quenching efficiency under the independent scattering approximation. These discrepancies indicate that additional mechanisms play a dominant role in limiting the performance of SHU metasurfaces.

## 5. Multiple-scattering effects

To investigate the impact of multiple scattering on the quenching efficiency, we perform full-wave electromagnetic simulations using the open-source software RETICOLO [36], which is

based on the rigorous coupled-wave analysis (RCWA) [37]. All simulations are carried out at a wavelength of  $\lambda = 532$  nm under normal incidence.

Owing to computational loads, SHU patterns containing only  $N = 26$  points are generated. Silicon nanoboxes with lateral dimensions of 100 nm and height of 145 nm, as in the experiment, are placed at the SHU coordinates on a silica substrate (see Figure S8–S9).

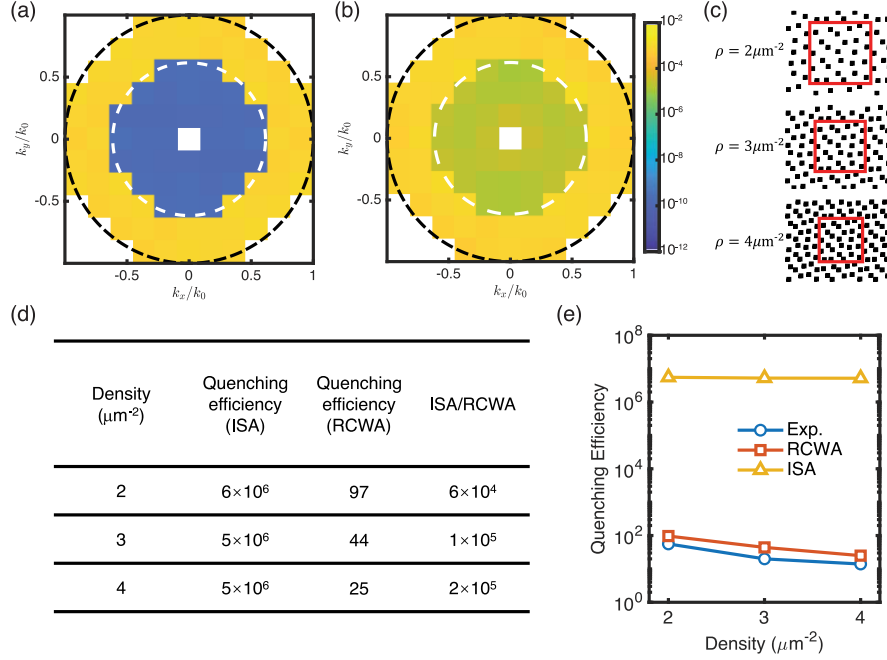


**Figure 6.** Impact of multiple scattering on quenching efficiency. (a) Reflected diffraction efficiencies in all orders of a 2D grating with a SHU unit cell containing  $N = 26$  Si identical nanoboxes computed under the independent scattering approximation (ISA) for  $\rho = 3 \mu\text{m}^{-2}$  and  $\chi = 0.35$ . Each diffraction order is represented by a square box. White boxes correspond to evanescent orders with in-plane wavenumber larger than the free space wavenumber  $k_0 = 2\pi/\lambda$ . The diffraction efficiency in the (0,0) order (specular light) is also represented as a white box. (b) RCWA results (multiple scattering is taken into account) for the same SHU pattern as in (a). (c) Schematic illustration of unit cells for SHU patterns with identical arrangements  $\chi = 0.35$  at different densities. (d) Calculated quenching efficiency of SHU metasurfaces as a function of density. As the density increases, the deviation from the ISA prediction becomes more pronounced. (e) Comparison between quenching efficiencies obtained from experiment, RCWA simulations, and ISA predictions. Data in (d) and (e) are obtained by averaging over 40 statistically independent realizations of patterns generated with the SHU generator. See Figure S8–S11 for more details, including convergence tests on the accuracy of the computed data.

Figure 6(a)-(b) show the computed diffraction efficiencies of all reflected diffraction orders of a SHU metasurface with density  $\rho = 3 \mu\text{m}^{-2}$  and  $\chi = 0.35$ . Each efficiency is represented with a square box and the two axes correspond to the in-plane wavevector components  $k_x$  and  $k_y$  normalized by the free-space wavenumber  $k_0$ . The supercell size is  $L = \sqrt{N/\rho} \approx 5.53\lambda$ . The white dashed circles indicate the quenching boundary predicted by Equation (4), while the black dashed circles represents the air light line,  $k_x^2 + k_y^2 = k_0^2$ .

The diffraction efficiencies computed with RETICOLO are displayed in Figure 6(b). For comparison, we also compute the diffraction efficiencies under the independent scattering approximation. The form factor of a single metaatom is obtained via RETICOLO by computing the diffraction efficiencies of a 2D grating formed by a single metaatom within the same supercell (see methods). The structure factor is calculated using Equation (2). The diffraction efficiencies are calculated as the product of the density, the form factor and the structure factor. The ISA results are as shown in Figure 6(a).

In both Figure 6(a) and 6(b), the abrupt transition predicted by the quenching equation is clearly observed. However, the quenching efficiency obtained from full-wave RCWA simulations is reduced by approximately five orders of magnitude compared to the independent-scattering-approximation prediction, highlighting the critical role of multiple scattering.

From a physical standpoint, multiple scattering effects are expected to become more pronounced as the metaatom density increases. This trend is confirmed experimentally: Figure S3 shows the measured bidirectional reflectance distribution function (BRDF) of SHU metasurfaces with identical degrees of stealthiness ( $\chi = 0.35$ ) but different densities ( $\rho = 2, 3$  and  $4 \mu\text{m}^{-2}$ ). As the density increases, the quenching efficiency decreases.

To quantitatively analyze the influence of density on multiple scattering, we uniformly rescale the coordinates of a fixed SHU pattern containing 26 points to generate metasurfaces with different target densities, see Figure 6(c). This procedure preserves the structure factor as a function of the reduced in-plane wavevector  $q_{\parallel}/\sqrt{\rho}$ . RCWA simulations are then performed for each density using the same supercell pattern.

Figure 6(d) compares the quenching efficiencies computed using RCWA, which fully accounts for multiple scattering, with those obtained using the independent scattering approximation for three different densities. The RCWA results exhibit a reduction in quenching efficiency of order  $10^5$  relative to the ISA predictions, with the discrepancy increasing at higher densities. In contrast, independent scattering approximation predicts a quenching efficiency that is essentially independent of density.

Figure 6(e) summarizes the experimental measurements together with the corresponding RCWA simulations and independent scattering approximation predictions for SHU metasurfaces at various densities. Taken together, these results demonstrate that multiple scattering imposes an intrinsic limitation on the achievable quenching efficiency of SHU metasurfaces. Even in the thermodynamic limit[**Erreur ! Source du renvoi introuvable.**]—where the system size tends to infinity and all metaatoms are assumed to be identical—the structure-factor-based predictions of SHU pattern generators break down due to unavoidable electromagnetic coupling between neighboring scatterers.

## Outlook

In SHU design, the art of programming consists in accurately positioning points to control interference in momentum space. With state-of-the-art SHU patterning algorithms, it is possible to engineer either destructive or constructive interference with high accuracy over a broad range of momentum patterns by positioning millions of points.

We used these algorithms to design periodic optical metasurfaces with SHU unit cells. The metasurfaces were fabricated using electron-beam lithography and reactive ion etching, resulting in SHU arrays of silicon nanoboxes on a silica substrate.

Our measurements show that the diffuse light exhibits a pronounced quenching around the specular direction, with an angle-dependent threshold that systematically satisfies the quenching equation [Equation (3)]. However, the experimentally observed quenching efficiency remains significantly lower than the theoretical values predicted from structure-factor computations.

We systematically investigated three possible origins of this discrepancy. First, achieving high quenching efficiency requires the fabrication of extremely large SHU patterns, on the order of  $10^{10}$  points, corresponding to an area of  $10^4 \text{ mm}^2$  for a density of  $2 \mu\text{m}^{-2}$ . Second, polydispersity is a critical limitation. Even for simple metaatoms such as silicon nanoboxes, size-induced variations in the scattered field can introduce a significant amount of diffuse light within the quenching zone. Within experimental fabrication tolerances, we find that phase

variations have a more pronounced impact than amplitude variations. Third, we show that multiple scattering significantly limits the achievable quenching efficiency, even at densities commonly considered low for photonic applications (e.g.,  $2 \mu\text{m}^{-2}$ ).

We do not believe that there is substantial room for maneuver to overcome these limitations. Multiple scattering may be mitigated through the use of metaatoms with tailored shapes [38], and regular patterns with large  $\chi$  values represent a reliable alternative, as demonstrated here. The impact of polydispersity can be reduced by employing non-resonant metaatoms; however, this comes at the expense of a reduced diffuse-light signal. From an algorithmic perspective, it may be advantageous to develop new approaches that target lower quenching efficiencies in constrained wavevector regions, potentially offering greater robustness in unconstrained regions.

In the best experiment, we observed a quenching efficiency of 70, with typical values ranging from 10 to 30. For many light-harvesting applications, e.g. solar energy [30], such performance is satisfactory. However, for display-type applications, the achieved level of transparency may not be sufficient for the human eye, which is highly sensitive to noise.

## Methods

**Sample fabrication.** The metasurfaces were fabricated by etching structures into a 145 nm-thick polycrystalline silicon (Si-poly) layer. First, Si-poly was deposited on both sides of a 4-inch fused silica (FS) wafer by LPCVD at 605 °C. The Si-poly on one side of the wafer was then removed using fluorine-based reactive ion etching (F-RIE). The sample was subsequently coated with a 160 nm-thick layer of negative resist (maN2405, Micro Resist Technology) and a 40 nm-thick conductive layer (ELECTRA92, AllResist) to suppress charging during electron-beam lithography (EBL).

Patterns were exposed using EBL with a beam energy of 20 keV, a current of 135 pA, a step size of 4 nm, and a nominal dose of 150  $\mu\text{C}/\text{cm}^2$ . The resist was developed in MF-CD-26 (Microposit) at 20 °C for 50 s, rinsed with deionized water for 1 minute, and dried with nitrogen. The negative maN resist patterns were then transferred into the Si-poly layer using F-RIE, and the remaining resist mask was removed by oxygen plasma.

**Optical Characterization.** Images of the samples were acquired in bright-field mode using a Nikon 100× objective and a camera (Imaging Source, DFK 33UX264). BRDF measurements are conducted using a custom-built goniophotometer setup equipped with a supercontinuum laser and a 1 mm-diameter optical fiber connected to a spectrometer. The incidence ( $\theta_i$ ) and scattering ( $\theta_s, \phi_s$ ) angles are precisely controlled by three stepper motor rotation stages (Newport URS75, URS150, and SR50CC). As shown in Figure S1, the scattered light was collected slightly above the plane of incidence by a 1 mm diameter optical fiber connected to a spectrometer (Ocean Insight, HDX). The BRDF values were calibrated by measuring a Lambertian reflector with a reflectance of 99.99%, Spectralon (Labsphere SRS-99-010), using the same experimental setup.

**Electromagnetic computational results.** To compute the radiation diagrams of a single Si metaatom shown in Figure 5, we first used COMSOL Multiphysics 6.3 to calculate the near-field electromagnetic response of an isolated silicon nanobox placed on a silica substrate. The refractive index of silicon was taken from experimentally measured values,  $n_{\text{Si}} = 4.3 + 0.16i$ , while the refractive index of the silica substrate was set to 1.46. The open-source software RETOP [33] was then employed to perform the near-to-far-field transformation, yielding the plane-wave expansion of the far-field radiation for Si nanoboxes of different sizes.

For the results presented in Figure 6, each supercell consists of 26 Si metaatoms arranged on a silica substrate, with air as the superstrate. The diffraction efficiencies in all orders are

computed using the open-source software RETICOLO [36]. To ensure numerical convergence, at least  $81 \times 81$  Fourier harmonics are retained in the calculations. Simulations are performed under normal incidence, and the total diffraction efficiency is obtained by averaging the TE and TM polarization contributions for each diffraction order.

For the corresponding independent-scattering-approximation calculations, a single Si nanobox is placed at the center of a supercell of identical size. The diffraction efficiencies of all orders are again computed using RETICOLO, with the same number of retained Fourier harmonics to avoid numerical discrepancies. These single-particle diffraction efficiencies are then multiplied by the numerically computed structure factor of each SHU pattern, as defined in Equation (2). This approach allows the ISA predictions to be obtained very efficiently while maintaining the same level of numerical accuracy as the full RCWA calculations.

## Acknowledgements

PL acknowledges financial support from the Grand Research Program LIGHT Idex of Bordeaux University and the European Research Council Advanced grant (Project UNSEEN No. 101097856). The authors thanks Philippe Teulat for his repeated help in developing the goniospectrometer setup. They acknowledge fruitful interactions with Louis Forestier. Sample fabrication was supported by LAAS-CNRS micro and nanotechnologies platform, a member of the RENATECH French national network.

## Competing interests

The authors declare no competing interests.

## References

1. P. Sheng, *Introduction to Wave Scattering, Localization and Mesoscopic Phenomena* (Academic, 1995).
2. P. Sebbah, *Waves and Imaging through Complex Media* (Kluwer Academic, 2001).
3. K. Vynck, R. Pierrat, R. Carminati, L. S. Froufe-Pérez, F. Scheffold, R. Sapienza, S. Vignolini, and J. J. Sáenz, "Light in correlated disordered media", *Rev. Mod. Phys.* **95**, 045003 (2023).
4. K. Vynck, R. Pacanowski, A. Agreda, A. Dufay, X. Granier, and P. Lalanne, "The visual appearances of disordered optical metasurfaces", *Nat. Mater.* **21**, 1035–1041 (2022).
5. D. Arslan, A. Rahimzadegan, S. Fasold, et al., "Toward perfect optical diffusers: dielectric Huygens' metasurfaces with critical positional disorder", *Adv. Mater.* **34**, 2105868 (2022).
6. P. M. Piechulla, B. Fuhrmann, E. Slivina, et al., "Tailored light scattering through hyperuniform disorder in self-organized arrays of high-index nanodisks", *Adv. Opt. Mater.* **9**, 2100186 (2021).
7. P. M. Piechulla, Y.J. Donie, R.B. Wehrspohn, U. Lemmer, G. Gomard, A.N. Sprafke, "Correlated Disorder Substrate-Integrated Nanodisk Scatterers for Light Extraction in Organic Light Emitting Diodes", *Adv. Opt. Mater.* **11**, 2202557 (2023).
8. T. Tani, S. Hakuta, N. Kiyoto, and M. Naya, "Transparent near-infrared reflector metasurface with randomly dispersed silver nanodisks", *Opt. Express* **22**, 9262–9270 (2014).
9. Y. Billiet, V. Chevalier, S. Kostcheev, H. Kadiri, S. Blaize, A. Rumyantseva, and G. Lérondel, "Engineering of diffuse structural colors", *Adv. Opt. Mater.* **12**, 2302165 (2024).
10. S. Torquato and F. H. Stillinger, "Local density fluctuations, hyperuniformity, and order metrics," *Phys. Rev. E* **68**, 041113 (2003).

11. R. D. Batten, F. H. Stillinger, S. Torquato, "Classical disordered ground states: Super-ideal gases and stealth and equi-luminous materials," *J. Appl. Phys.* **104**, 033504 (2008).
12. M. Castro-Lopez, M. Gaio, S. Sellers, G. Gkantzounis, M. Florescu, and R. Sapienza, "Reciprocal space engineering with hyperuniform gold disordered surfaces", *APL Photonics* **2**, 066103 (2017).
13. S. Gorsky, W. A. Britton, Y. Chen, J. Montaner, A. Lenef, M. Raukas, and L. Dal Negro, "Engineered hyperuniformity for directional light extraction", *APL Photonics* **4**, 111101 (2019).
14. Y. Jiao, T. Lau, H. Hatzikirou, M. Meyer-Hermann, J. C. Corbo, and S. Torquato, "Avian photoreceptor patterns represent a disordered hyperuniform solution to a multiscale packing problem", *Phys. Rev. E* **89**, 022721 (2014).
15. O. H. Philcox and S. Torquato, "Disordered heterogeneous universe: Galaxy distribution and clustering across length scales", *Phys. Rev. X* **13**, 011038 (2023).
16. L. S. Froufe-Pérez, M. Engel, P. F. Damasceno, N. Muller, J. Haberk, S. C. Glotzer, and F. Scheffold, "Hyperuniformity in the Formation of Band Gaps in Disordered Photonic Materials", *Phys. Rev. Lett.* **117**, 053902 (2016).
17. L. S. Froufe-Pérez, G. J. Aubry, F. Scheffold, and S. Magkiriadou, "Bandgap fluctuations and robustness in two-dimensional hyperuniform dielectric materials", *Opt. Express* **31**, 18509–18515 (2023).
18. M. Diego, J. Hardouin, G. Mazevert-Schagrod, M. Pirro, B. Kim, R. Anufriev, and M. Nomura, "Hypersonic acoustic wave control via stealthy hyperuniform phononic nanostructures", *Sci. Adv.* **11**, eadw7205 (2025).
19. G. J. Aubry, L. S. Froufe-Pérez, U. Kuhl, O. Legrand, F. Scheffold, and F. Mortessagne, "Experimental tuning of transport regimes in hyperuniform disordered photonic materials," *Phys. Rev. Lett.* **125**, 127402 (2020).
20. P. Lalanne, M. Chen, C. Rockstuhl, A. Sprafke, A. Dmitriev, K. Vynck, "Disordered optical metasurfaces: basics, design and applications", *Adv. Opt. Photon.* **17**, 45-112 (2025).
21. H. Zhang, et al., "Hyperuniform disordered distribution metasurface for scattering reduction," *Appl. Phys. Lett.* **118**, 101101 (2021).
22. P. K. Morse, J. Kim, P. J. Steinhardt, and S. Torquato, "Generating large disordered stealthy hyperuniform systems with ultra-high accuracy to determine their physical properties", *Phys. Rev. Research* **5**, 033190 (2023).
23. F. Chehami, C. Decroze, T. Pasquet, E. Perrin, and T. Fromenteze, "Morphogenetic Design of Self-Organized Correlated Disordered Electromagnetic Media", *ACS Photonics* **10**, 1890-1898 (2023).
24. A. Shih, M. Casiulis, S. Martiniani, "Fast Generation of Spectrally-Shaped Disorder", *Phys. Rev. E* **110**, 034122 (2024).
25. S. Yu, C.-W. Qiu, Y. Chong, S. Torquato, and N. Park, "Engineered disorder in photonics", *Nat. Rev. Mater.* **6**, 226–243 (2021).
26. O. Leseur, R. Pierrat, and R. Carminati, "High-density hyperuniform materials can be transparent," *Optica* **3**, 763–767 (2016).
27. S. Torquato, G. Zhang, and F. H. Stillinger, "Ensemble theory for stealthy hyperuniform disordered ground states", *Phys. Rev. X* **5**, 021020 (2015).
28. M. Chen, A. Agreda, T. Wu, F. Carcenac, K. Vynck, P. Lalanne, "Emergent scattering regimes in disordered metasurfaces near critical packing", *Nat. Commun.* **16**, 11125 (2025).
29. A. Agreda, T. Wu, A. Hereu, M. Treguer-Delapierre, G. L. Drisko, K. Vynck, P. Lalanne, "Tailoring iridescent visual appearance with disordered resonant metasurfaces," *ACS Nano* **17**, 6362–6372 (2023).
30. N. Tavakoli, R. Spalding, P. Koppejan, G. Gkantzounis, C. Wang, R. Röhrich, E. Kontoleta, A.F. Koenderink, R. Sapienza, M. Florescu, E. Alarcon-Llado, "Over 65%

Sunlight Absorption in a 1  $\mu\text{m}$  Si Slab with Hyperuniform Texture", ACS Photonics **9**, 1206-17 (2022).

- 31. S. Divitt and L. Novotny, "Spatial coherence of sunlight and its implications for light management in photovoltaics", Optica **2**, 95–103 (2015).
- 32. J. W. Goodman, Introduction to Fourier Optics (Ben Roberts, 2005), 3rd ed.
- 33. J. Yang, J. P. Hugonin, P. Lalanne, "Near-to-far field transformations for radiative and guided waves," ACS Photonics **3**, 395–402 (2016).
- 34. V. Romero-García, N. Lamothe, G. Theocharis, O. Richoux, L. M. Garcia-Raffi, "Stealth acoustic materials," Phys. Rev. Appl. **11**, 054076 (2019).
- 35. A. Rohfritsch, J. M. Conoir, T. Valier-Brasier, R. Marchiano, "Impact of particle size and multiple scattering on the propagation of waves in stealthy-hyperuniform media," Phys. Rev. E **102**, 053001 (2020).
- 36. J. P. Hugonin, P. Lalanne, "RETICOLO software for grating analysis", arXiv:2101.00901 (2021)
- 37. L. Li, "New formulation of the Fourier modal method for crossed surface-relief gratings", J. Opt. Soc. Am. A **14**, 2758–2767 (1997).
- 38. C. Gigli, Q. Li, P. Chavel, G. Leo, M. L. Brongersma, P. Lalanne, "Fundamental limitations of Huygens' metasurfaces for optical beam shaping," Laser Photon. Rev. **15**, 2000448 (2021).